https://doi.org/10.1016/j.cplett.2019.137039

Preparation and photoelectric properties of SnO_x films with tunable optical bandgap

Fang Wang[a,b,c], Menghan Jia[a,b,c], Libin Tang[b,c,*], Chong Wang[a,*], Jinzhong Xiang[d,*], Kar Seng Teng[e,*], Shu Ping Lau[f]

[a] *School of Materials Science and Engineering, Yunnan University, Kunming 650091, China*

[b] *Kunming Institute of Physics, Kunming 650223, China*

[c] *Yunnan Key Laboratory of Advanced Photoelectric Materials & Devices, Kunming 650223, China*

[d] *School of Physics and Astronomy, Yunnan University, Kunming 650091, China*

[e] *College of Engineering, Swansea University, Bay Campus, Fabian Way, Swansea SA1 8EN, United Kingdom*

[f] *Department of Applied Physics, The Hong Kong Polytechnic University, Hung Hom, Kowloon, Hong Kong, China*

Highlights:

1. Tunable optical band gap of SnO_x films prepared using RF magnetron sputtering at different oxygen partial pressures and heat treatment.
2. Broad optical absorption bands of SnO_x thin films covering UVA, UVB and UVC.
3. Fabrication of UV photodetector based on the SnO_x film.

Abstract: SnO_x thin films with tunable optical bandgap were prepared using RF magnetron sputtering. The bandgap was adjustable between 2.16 and 3.96 eV depending on oxygen partial pressure during deposition and heat treatment. The structure and properties of the SnO_x films were studied. The optical absorption of the SnO_x films covered multiple ultraviolet bands, such as UVA, UVB and UVC. A photodetector based on the annealed SnO_x film exhibited a detectivity of 1×10^{11} Jones

(under 365 nm UV light) at room temperature, which demonstrates the important potential application of SnO_x films for UV detection.

Keywords: SnO_x, Oxygen partial pressure, Tunable optical band gap, Ultraviolet detection

1. Introduction

Ultraviolet (UV) photodetector can find many applications, such as fire detection, ozone monitoring, chemical analysis and defense technology etc. Due to the relatively large photon energy of UV light, wide bandgap semiconductor materials, such as ZnO[1-3], Ga_2O_3[4-6], SiC[7-8], GaN[9-10] and MgO[11] etc, are commonly used in the production of UV photodetectors. The extensive research into wide bandgap semiconductors has led to the emergence of new material systems, such as stannous oxide (SnO) and tin oxide (SnO_2), suitable for UV photodetection. SnO is a p-type semiconductor material with a direct bandgap of 2.7 eV[12-13]. The main reason for the p-type conductivity of SnO is due to the presence of Sn vacancies and the oxidized state of Sn^{2+} occupying the gap position of oxygen atoms. The 2p core level of O and 5s core level of Sn are close to the valence band maximum (VBM), hence easing orbital hybridization resulting in the enhancement of hole transport[14]. On the other hand, SnO_2 is a typical n-type metal oxide semiconductor material with a direct bandgap of 3.6 eV. It has the same elements as SnO but in different proportions. Furthermore, it exhibited many excellent properties and is widely used in the fields of catalysis[15], gas sensor[16], energy storage[17], solar cell[18] and so on.

Currently, the main preparation methods of tin oxide include electrospinning[19], pulsed laser deposition[20], hydrothermal[21], molecular beam epitaxy and magnetron sputtering[22] etc. Among these methods, magnetron sputtering has the advantages of simple operation, good uniformity as well as excellent repeatability on device performance. In this paper, SnO_x film was prepared using radio frequency (rf) magnetron sputtering combined with high temperature treatment. The use of the film

for UV photodetection was investigated.

2. Experimental

2.1. Preparation and annealing of SnO_x films

Substrates (Quartz, SiO_2/Si, ITO) were cleaned with deionized water, dried with high-purity nitrogen, and immediately placed in a vacuum chamber at 4.0×10^{-4} Pa. SnO material was used as target (99.99 %, Zhongnuo New Material (Beijing) Technology Co. Ltd.). Different oxygen partial pressure (O_{pp}) of 12, 10, 8 and 0 % were studied by controlling the flow of O_2 and Ar gas. The thickness of the films can be tuned by adjusting sputtering power and time, in this work sputtering power and time of 120 W and 40 min was used during deposition, respectively. The deposited film was annealed at 300 ℃ for 1 h in a tubular furnace under atmospheric pressure to control the optical band gap of the material. After annealing, there was a slight change in the color of the sample. The samples were cooled to room temperature before performing characterization on the films.

2.2. Characterization of the thin film

The crystallinity of the film was characterized by X-ray diffraction (XRD, model: EMPYREAN) and transmission electron microscope (TEM, model: JEM-2100). Its elemental composition was studied using X-ray photoelectron spectroscopy (XPS, model: K-Alpha$^+$, Mono Al k-alpha). The surface morphology and thickness of the film were analyzed using atomic force microscope (AFM, model number: SPA-400). The optical properties of the film were characterized using UV-Vis spectrometer (model: iHR-320). All measurements were conducted at room temperature.

2.3. Fabrication and characterization of SnO_x photodetector

A photodetector, consisting of quartz/SnO_x/Ag structure, was fabricated and characterized. The annealed SnO_x film with O_{pp} of 10% was chosen as the

photosensitive material. Current density against voltage (*J-V*) characteristic curve of the photodetector were measured using Keithley 2400. This allowed the determination of photogeneration current, responsivity rate and detectivity of the photodetector.

3. Results and discussion

A schematic diagram of the deposition process of SnO_x film using rf magnetron sputtering is shown in Fig. 1(a). The film was deposited on quartz substrate in a constant pressure of 0.6 pa with regulated O_{pp} by controlling the O_2 and Ar gas flow. Fig. 1(b) show the optical images of the SnO_x film on quartz substrate before (left image) and after (right image) annealing at 300 ℃ for 1 h, which the film appeared light purple in color and transparent with good transmission of light, respectively. XRD spectra, shown in Fig 1(c), were measured from annealed SnO_x films deposited on silicon substrates with different O_{pp} of 12, 10, 8 and 0 % indicated as Sample 1, 2, 3 and 4, respectively. At 0 % O_{pp} (i.e. pure argon with no oxygen), the XRD spectrum of Sample 4 showed preferential growth at (110) crystal plane of SnO (JCPDS No24.1342) with relatively large half-peak width, which suggests poor crystallinity of the film. With an increase of O_{pp}, the half-peak width of the diffraction peak of SnO in the direction of (110) was reduced hence indicating an improvement in its crystallinity. Furthermore, the square phase of SnO_2 (JCPDS No 46.1088) was also evident and revealed selectively growth on the (110) crystal surface. The SnO_x films deposited on the quartz substrates at different O_{pp} were characterized using UV-Vis absorption spectroscopy, which allowed the determination of optical bandgap of the films using the geometric Tauc formula (Equation 1):

$$(\alpha h\nu)^2 \propto (h\nu - E_g) \quad (1)$$

where α is absorption coefficient, $h\nu$ is incident photon energy (eV), and E_g is optical bandgap. The optical bandgap of the annealed film with different O_{pp} of 0, 8 and 10 % can be estimated from fitting the linear part of the curves shown in Fig. 1(d) I, II and III, respectively. There was an increase in the optical bandgap after annealing of

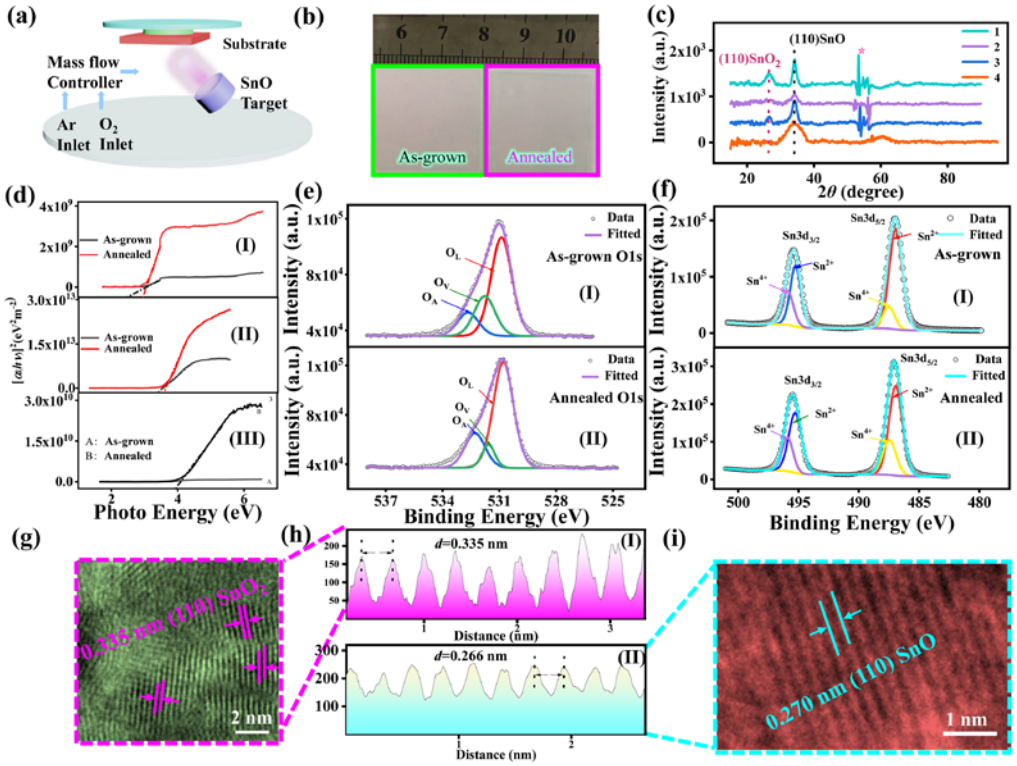

Fig. 1. (a) Schematic diagram illustrating magnetron sputtering deposition. (b) Optical images of SnO_x films deposited on quartz substrates. (c) XRD patterns of SnO_x films on (100) plane SiO_2/Si substrate deposited with different O_{PP}. (d) Tauc plots for estimating optical bandgap of SnO_x films. (e), (f) O1s and Sn3d XPS spectra of the SnO_x films, respectively. (g) TEM image of SnO_2. (h) Line profiles of lattice fringes of SnO_2 and SnO are shown in I and II, respectively. (i) TEM image of SnO.

the film as well as increasing O_{pp} during film deposition, which suggests that the optical bandgap can be adjustable between 2.16 and 3.96 eV. The formation of SnO_x crystal depends on the bonding of Sn and O atoms. At low O_{pp}, Sn-O bonds are formed in the crystal lattice but there are still many Sn atoms that are not bonded with O atoms, hence resulting in many vacancy sites in the SnO_2 and SnO lattices. These Sn atoms have weak localized electrons, which would change the electronic density of state of the film, resulting in the decrease of the optical bandgap. After annealing, there was an increase in optical bandgap of all samples as pure Sn was volatilized at elevated temperature causing more Sn and O atoms to bond covalently.

The elemental composition and chemical bond of the deposited SnO_x film with O_{pp} of 10 % was investigated before and after annealing using XPS. Fig. 1(e) shows the

fitted curves of O1s XPS spectra of the SnO_x film before and after annealing (indicated as I and II in the figure, respectively). The as-grown film consisted of a high proportion of lattice oxygen (O_L), followed by vacancy oxygen (O_V) and then adsorbed oxygen (O_A) at a ratio of 1: 0.41: 0.24 (O_L: O_V: O_A). After annealing, it was evident that there was a significant reduction in O_V and an increase in the proportion of O_L resulting in a ratio of 1: 0.22: 0.33 (O_L: O_V: O_A), hence suggesting an increase in the formation of Sn-O bonds. Fig. 1(f) shows the fitted curves of Sn $3d_{5/2}$ and Sn $3d_{3/2}$ XPS spectra of the film. The fitted Sn^{2+} peak was larger than the Sn^{4+} peak in both conditions. However, during annealing oxygen may oxidize a part of Sn^{2+} to Sn^{4+}, resulting the proportion of the Sn^{4+} peak increased from 0.30 to 0.36 after annealing.

TEM images of annealed SnO_2 and SnO films are shown in Fig. 1(g) and (i), respectively. Both films exhibited lattice fringes, which demonstrated good crystallinity after annealing. The line profiles of SnO_2 and SnO lattice fringes are shown in Fig. 1(h-I) and (h-II), respectively. The interplanar spacing of SnO_2 was d = 0.335 nm and that of SnO was d = 0.266 nm, which is very close to the value of 0.270 nm spacing of PDF standard (110). The results were also consistent with those of XRD.

Fig. 2(a) shows high resolution TEM image of SnO_x film, which consisted of SnO and SnO_2 on the left (shaded in green) and right (shaded in red), respectively. The corresponding atomic model diagram of the green shaded area observed from the top is shown in Fig. 2(b). The black rectangular line is associated with the position of Sn^{2+}, which belongs to the orthorhombic crystal system (a=3.82 nm, b=3.61 nm, c=4.30 nm) of pm21n space group. The atomic model diagram corresponding to the red shaded area from the top is shown in Fig. 2(c). There is a consistent lattice fringe of SnO_2 observed from the crystal orientation [001] downward. The crystal plane spacing measured in (110) is 0.335 nm, which is consistent with the interplanar spacing measurement from the TEM in Fig. 1(g). Another orientation of SnO_2 was observed (as shown in Fig. 2(d)) similar to the crystal orientation of [010]. The measured spacing at the crystal planes of (101) and (200) were 0.264 and 0.237 nm, respectively. As the SnO_2 belongs to the tetragonal system (a=4.75 nm, b=4.75 nm, c=3.19 nm), an addition of odd index in the

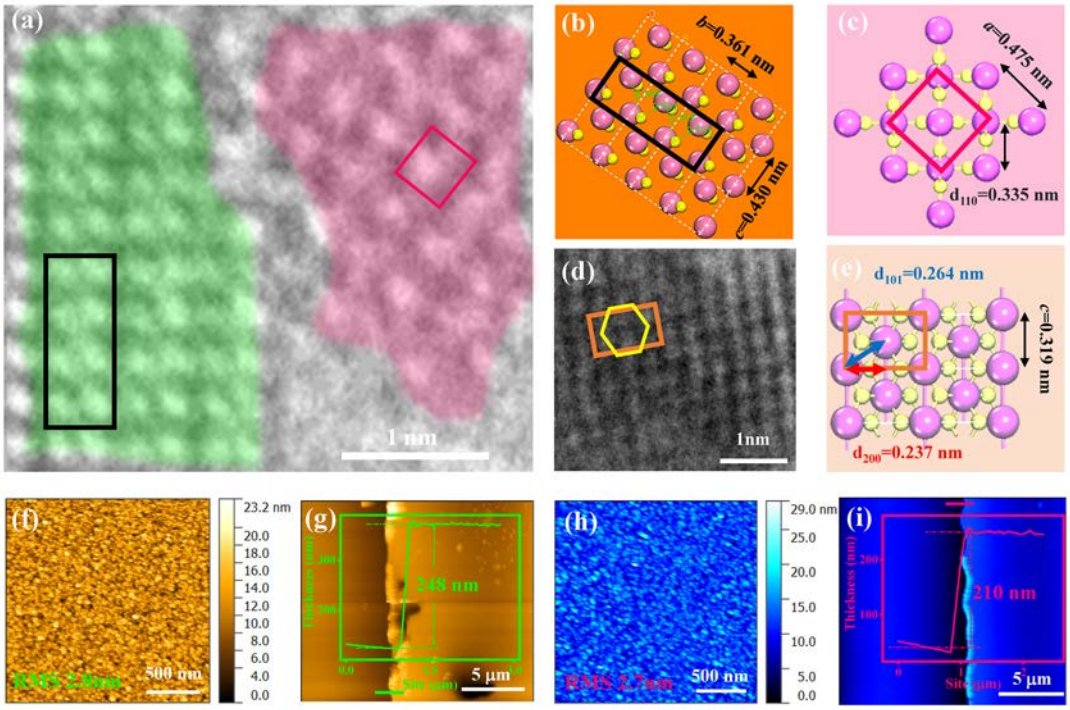

Fig. 2. (a) HRTEM image of SnO_x films. (b), (c) Schematic atomic model of SnO and SnO_2 films from top view corresponding to the green and red shaded areas in (a), respectively. (d), (e) HRTEM image of SnO_2 film and corresponding schematic atomic model from top view, respectively. (f) AFM topographical image of as-grown SnO_x film. (g) AFM line profile across a step edge (green line) of as-deposited SnO_x film. (h) AFM topographical image of annealed SnO_x film. (i) AFM line profile across a step edge (red line) of annealed SnO_x film.

crystal plane would result in an extinction phenomenon, which would obscure the (100) crystal plane. Fig. 2(e) shows the corresponding atomic model diagram, which Sn^{4+} occupies the vertices and focal points of the orange rectangular line, and O^{2-} exhibits a hexagonal arrangement.

Surface morphology of the SnO_x film with O_{pp} of 10 % was studied using AFM to determine the quality of film formation as it will affect the optical properties of the material. Fig. 2(f) shows the AFM topographical image of the as-grown SnO_x film. The root-mean-square (RMS) roughness of the film was 2.8 nm. Wet etching was carried out on the as-grown film in order to perform step measurements to determine the film thickness. Fig. 2(g) shows the AFM line profile across the step and revealed a film thickness of 240 ± 4.9 nm. The AFM image of the film after annealing is shown in Fig. 2(h). There was no obvious change in the RMS roughness of the annealed film.

However, the film thickness was reduced by 40 nm after annealing as shown in Fig. 2(i). This could be due to densification and crystallization, which would result in a much denser film[23]. Such phenomena would have certain impact on the optical and electrical properties of the film.

UV photodetectors based on the SnO_x films were fabricated and have a device structure of quartz/SnO_x/Ag as shown in Fig. 3(a). The SnO_x films were deposited with 0 % , 8% and 10% O_{pp} on quartz substrates and annealed at 300 °C for 1 h, it was found that only 10% O_{pp} may lead to a stable device performance, thus it has been chosen to fabricate the photodetector. Fig. 3(b) illustrates the working principle of the photodetector using an energy band diagram. A p-n junction was formed between p-type SnO (E_g = 2.7 eV) and n-type SnO_2 (E_g = 3.6 eV) semiconductor materials. When the device is exposed to 365 nm UV light, electrons would migrate from SnO to SnO_2 (and holes migrate from SnO_2 to SnO) hence resulting in a potential difference that would generate a photocurrent in a closed circuit. *J*-*V* and log *J*-*V* characteristic curves of the device are shown in Fig. 3(c) and (d), respectively. Both plots showed that the photocurrent (under 365 nm UV light at a power density of 0.185 mW/cm^2) was larger than the dark current, thus the device was suitable for UV detection. Responsivity (*R*) is an important parameter that reflects the performance of photodetector. It can be determined using the following formula (Equation 2):

$$R = \frac{J_{ph}}{P_{opt}} \tag{2}$$

where J_{ph} is photocurrent density and P_{opt} is photo power density. For a photo power density of 0.185 mW/cm^2, the maximum responsivity of the photodetector exceeded 0.9 A/W as shown in Fig. 3(e). Another important parameter is the detectivity (*D**), which can be determined using the following expression (Equation 3):

$$\boldsymbol{D^* = \frac{R}{2q\sqrt{|J_{dark}|}}} \tag{3}$$

where J_{dark} is dark current density, q is unit charge (1.6×10^{19} C). As shown in Fig. 3(f),

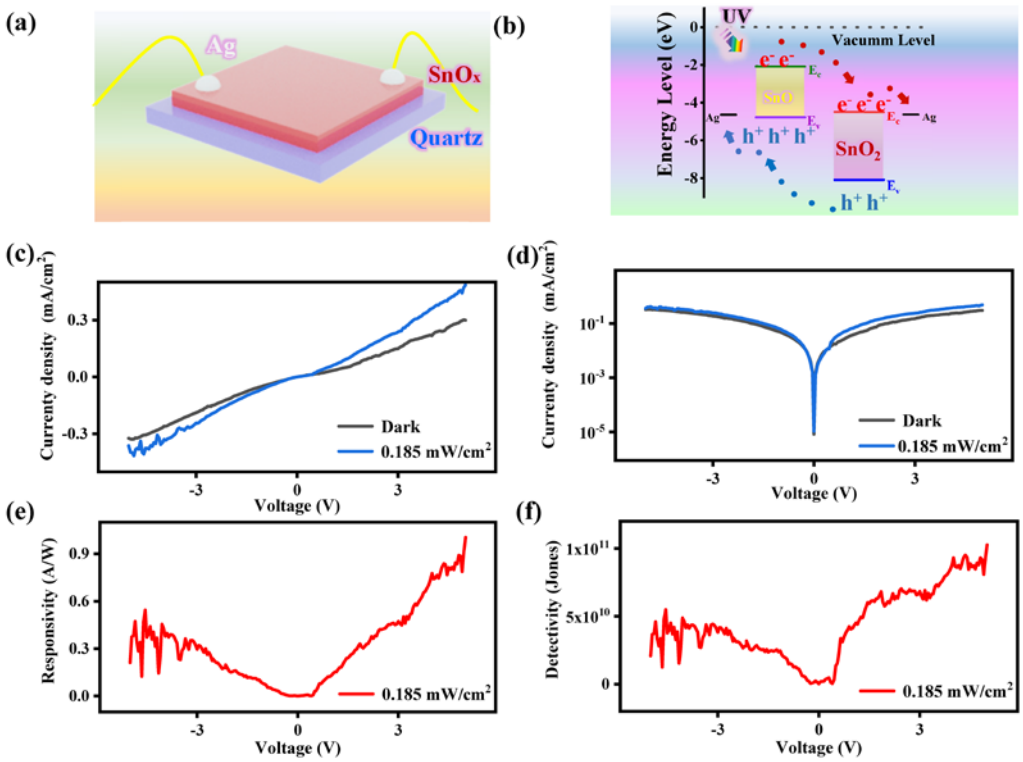

Fig. 3. (a) Schematic diagram of SnO_x based UV photoconductive detector. (b) Energy band diagram of the photodetector. (c), (d) Plots of *J–V* and log *J–V* characteristic curves of the photodetector based on SnO/SnO_2 film under 365 nm illumination, respectively. (e), (f) Plots of responsivity *(R) -V* and detectivity $(D^*) - V$ curves of the UV photodetectors based on the SnO/SnO_2 film.

*D** was stable at 10^{10} Jones (1 Jones = 1 cm· $Hz^{1/2}$·W^{-1}) and its highest value could reach 10^{11} Jones. Both the responsivity and detectivity of the photodetector were much higher under forward bias voltage[24-25].

4. Conclusion

SnOx thin films were prepared by magnetron sputtering. The bandgap of the film can be adjustable between 2.16 and 3.96 eV depending on the percentage of OPP during film deposition and heat treatment after growth. An unoptimized UV photodetector, consisting of quartz/SnO_x/Ag, was fabricated and exhibited a detectivity of 10^{11} Jones under 365 nm UV light. The adjustable bandgap of the SnO_x film would allow its use in UV light-emitting diodes and sunblind UV detectors.

Acknowledgments

This work was supported by the National Natural Science Foundation of China (Grant Nos. 61106098, 51201150, 11374250, and 11864044), the Key Project of Applied Basic Research of Yunnan Province, China (Grant No. 2012FA003), PolyU grants (1-ZVGH and 1-BBAD), and Research Grants Council of Hong Kong (Project Nos.: PolyU153030/15P, PolyU153271/16P, and PolyU 153039/17P).

References

1. Gong, M.; Liu, Q.; Cook, B.; Kattel, B.; Wang, T.; Chan, W. L.; Ewing, D.; Casper, M.; Stramel, A.; Wu, J. Z., All-Printable ZnO Quantum Dots/Graphene van der Waals Heterostructures for Ultrasensitive Detection of Ultraviolet Light. *ACS Nano* **2017,** *11* (4), 4114-4123.

2. Li, L.; Gu, L.; Lou, Z.; Fan, Z.; Shen, G., ZnO Quantum Dot Decorated Zn_2SnO_4 Nanowire Heterojunction Photodetectors with Drastic Performance Enhancement and Flexible Ultraviolet Image Sensors. *ACS Nano* **2017,** *11* (4), 4067-4076.

3. Zheng, Z.; Gan, L.; Zhang, J.; Zhuge, F.; Zhai, T., An Enhanced UV-Vis-NIR an d Flexible Photodetector Based on Electrospun ZnO Nanowire Array/PbS Quantum Dots Film Heterostructure. *Adv Sci (Weinh)* **2017,** *4* (3), 1600316.

4. Kong, W. Y.; Wu, G. A.; Wang, K. Y.; Zhang, T. F.; Zou, Y. F.; Wang, D. D.; Luo, L. B., Graphene-β-Ga_2O_3 Heterojunction for Highly Sensitive Deep UV Photodetector Application. *Adv Mater* **2016,** *28* (48), 10725-10731.

5. Li, P.; Shi, H.; Chen, K.; Guo, D.; Cui, W.; Zhi, Y.; Wang, S.; Wu, Z.; Chen, Z.; Tang, W., Construction of GaN/Ga_2O_3 p–n junction for an extremely high responsivity self-powered UV photodetector. *J. Mater. Chem. C* **2017,** *5* (40), 10562-10570.

6. Zou, R.; Zhang, Z.; Liu, Q.; Hu, J.; Sang, L.; Liao, M.; Zhang, W., High detectivity solar-blind high-temperature deep-ultraviolet photodetector based on multi-layered (l00) facet-oriented β-Ga_2O_3 nanobelts. *Small* **2014,** *10* (9), 1848-56.

7. Zhou, X.; Han, T.; Lv, Y.; Li, J.; Lu, W.; Wang, Y.; Song, X.; Tan, X.; Liang, S.; Feng, Z.; Cai, S., Large-Area 4H-SiC Ultraviolet Avalanche Photodiodes Based on Variable-Temperature Reflow Technique. *IEEE Electron Device Letters* **2018,** *39* (11), 1724-1727.

8. Kim, M.; Seo, J. H.; Zhao, D. Y.; Liu, S. C.; Kim, K.; Lim, K.; Zhou, W. D.; Waksc, E.; Ma, Z. Q., Transferrable single crystalline 4H-SiC nanomembranes. *Journal of Materials Chemistry C* **2017,** *5* (2), 264-268.

9. Wang, W.; Yang, Z.; Lu, Z.; Li, G., High responsivity and low dark current nonpolar GaN-based ultraviolet photo-detectors. *Journal of Materials Chemistry C* **2018,** *6* (25), 6641-6646.

10. R, A.; R, R.; R, L.; Vavilapalli, D. S.; Baskar, K.; Singh, S., Large area ultraviolet photodetector on surface modified Si:GaN layers. *Applied Surface Science* **2018,** *435*, 1057-1064.

11. Zhou, H.; Gui, P.; Yu, Q.; Mei, J.; Wang, H.; Fang, G., Self-powered, visible-blind ultraviolet photodetector based on n-ZnO nanorods/i-MgO/p-GaN structure light-emitting diodes. *Journal of Materials Chemistry C* **2015,** *3* (5), 990-994.

12. Li, K.-M.; Li, Y.-J.; Lu, M.-Y.; Kuo, C.-I.; Chen, L.-J., Direct Conversion of Single-Layer SnO Nanoplates to Multi-Layer SnO2Nanoplates with Enhanced Ethanol Sensing Properties. *Advanced Functional Materials* **2009,** *19* (15), 2453-2456.
13. Ogo, Y.; Hiramatsu, H.; Nomura, K.; Yanagi, H.; Kamiya, T.; Hirano, M.; Hosono, H., p-channel thin-film transistor using p-type oxide semiconductor, SnO. *Applied Physics Letters* **2008,** *93* (3).
14. Hsu, P. C.; Hsu, C. J.; Chang, C. H.; Tsai, S. P.; Chen, W. C.; Hsieh, H. H.; Wu, C. C., Sputtering deposition of P-type SnO films with SnO_2 target in hydrogen-containing atmosphere. *ACS Appl Mater Interfaces* **2014,** *6* (16), 13724-9.
15. Yang, Z.; Wang, H.; Song, W.; Wei, W.; Mu, Q.; Kong, B.; Li, P.; Yin, H., One dimensional SnO_2 NRs/Fe_2O_3 NTs with dual synergistic effects for photoelectrocatalytic reduction CO_2 into methanol. *J Colloid Interface Sci* **2017,** *486*, 232-240.
16. Verma, M. K.; Gupta, V., A highly sensitive SnO_2–CuO multilayered sensor structure for detection of H_2S gas. *Sensors and Actuators B: Chemical* **2012,** *166-167*, 378-385.
17. Wang, Z.; Song, D.; Si, J.; Jiang, Y.; Yang, Y.; Jiang, Y.; Huang, S.; Chen, Z.; Zhao, B., One-step hydrothermal reduction synthesis of tiny Sn/SnO_2 nanoparticles sandwiching between spherical graphene with excellent lithium storage cycling performances. *Electrochimica Acta* **2018,** *292*, 72-80.
18. Zhang, Q.; Cao, G., Nanostructured photoelectrodes for dye-sensitized solar cells. *Nano Today* **2011,** *6* (1), 91-109.
19. Cho, J. S.; Kang, Y. C., Nanofibers Comprising Yolk-Shell Sn@void@SnO/SnO_2 and Hollow SnO/SnO_2 and SnO_2 Nanospheres via the Kirkendall Diffusion Effect and Their Electrochemical Properties. *Small* **2015,** *11* (36), 4673-81.
20. Saji, K. J.; Tian, K.; Snure, M.; Tiwari, A., 2D Tin Monoxide-An Unexplored p-Type van der Waals Semiconductor: Material Characteristics and Field Effect Transistors. *Advanced Electronic Materials* **2016,** *2* (4).
21. Li, N.; Fan, Y.; Shi, Y.; Xiang, Q.; Wang, X.; Xu, J., A low temperature formaldehyde gas sensor based on hierarchical SnO/SnO2 nano-flowers assembled from ultrathin nanosheets: Synthesis, sensing performance and mechanism. *Sensors and Actuators B: Chemical* **2019,** *294*, 106-115.
22. Hota, M. K.; Hedhili, M. N.; Wang, Q.; Melnikov, V. A.; Mohammed, O. F.; Alshareef, H. N., Nanoscale Cross-Point Resistive Switching Memory Comprising p-Type SnO Bilayers. *Advanced Electronic Materials* **2015,** *1* (3).
23. Li, M.; Jin, Z. X.; Zhang, W.; Bai, Y. H.; Cao, Y. Q.; Li, W. M.; Wu, D.; Li, A. D., Comparison of chemical stability and corrosion resistance of group IV metal oxide films formed by thermal and plasma-enhanced atomic layer deposition. Sci Rep 2019, 9 (1), 10438.
24. Kim, H. S.; Patel, M.; Kim, J.; Jeong, M. S., Growth of Wafer-Scale Standing Layers of WS_2 for Self-Biased High-Speed UV-Visible-NIR Optoelectronic Devices. *ACS Appl Mater Interfaces* **2018,** *10* (4), 3964-3974.
25. Tang, R.; Han, S.; Teng, F.; Hu, K.; Zhang, Z.; Hu, M.; Fang, X., Size-Controlled Graphene Nanodot Arrays/ZnO Hybrids for High-Performance UV Photodetectors. *Adv Sci (Weinh)* **2018,** *5* (1), 1700334.